Resolvent analysis on a swirling turbulent jet

Quentin Chevalier, Christopher M Douglas, Lutz Lesshafft

Resolvent analysis on a swirling turbulent jet

Quentin Chevalier[1*], Christopher M. Douglas[1] and Lutz Lesshafft[1]

[1]Laboratoire d'Hydrodynamique, CNRS, Ecole polytechnique, Institut Polytechnique de Paris, Palaiseau, 91120, France.

*Corresponding author(s). E-mail(s): quentin.chevalier@polytechnique.edu;
Contributing authors: douglas@ladhyx.polytechnique.fr; lesshafft@ladhyx.polytechnique.fr;

Abstract

This study explores coherent structures in a swirling turbulent jet. A stationary axisymmetric solution of the Reynolds–Averaged Navier–Stokes equations at $\boldsymbol{Re = 200,000}$ was obtained using an open source computational fluid dynamics code and the Spalart–Allmaras eddy viscosity model. Resolvent analysis with the same eddy viscosity field then provided coherent structures of the turbulent fluctuations on the baseflow. As in many earlier studies, a large gain separation is identified between the optimal and sub-optimal resolvent modes, permitting a focus on the most amplified response mode and its corresponding optimal forcing. At zero swirl, the results indicate that the jet's coherent response is dominated by axisymmetric ($\boldsymbol{m = 0}$) structures, which are driven by the usual Kelvin-Helmholtz shear instability mechanism. However, as swirl is increased, different coherent structures begin to dominate the response. For example, double and triple spiral ($|\boldsymbol{m}| = \mathbf{2}$ and $|\boldsymbol{m}| = \mathbf{3}$) modes are identified as the dominant structures when the axial and azimuthal velocity maxima of the base flow are equal. In this case, distinct co- and counter-rotating $|\boldsymbol{m}| = \mathbf{2}$ modes experience vastly different degrees of amplification. The mechanics of this selection process involve several physical mechanisms contributing simultaneously in different regions of the mode. This is analysed in more detail by comparing the alignment between the wavevector of the dominant response mode and the principal shear direction of the base flow. Additional discussion also considers the development of structures along the exterior of the jet nozzle, which is related to the lift-up effect.

Keywords: Resolvent analysis, Turbulence, Jets, Rotating Flows

Acknowledgments

This work is supported by the *Direction Générale de l'Armement*, the CleanSky2 Joint Undertaking under the European Union's Horizon 2020 research and innovation programme under grant agreement No 785303, and innovation program under the Marie Skłodowska-Curie grant agreement No. 899987. Results reflect only the authors' view and none of the above are responsible for any use that may be made of the information it contains. A CC-BY public copyright licence has been applied by the authors to the present document and will be applied to all subsequent versions up to the Author Accepted Manuscript arising from this submission, in accordance with the grants' open access conditions.

1 Introduction

Swirling jets are shear flows characterized by the introduction of angular momentum into a concentrated axial stream, causing fluid particles to travel in spiraling trajectories along the jet axis. Such flows may be found for instance in combustion chambers, where swirl is typically used to enhance mixing and promote

flame stability. Despite their widespread use in the combustion industry, the behaviour of such flows remain incompletely understood, especially with regards to the dominant coherent turbulent structures. This study aims to describe such coherent structures in a turbulent swirling jet using resolvent analysis.

[10, 20, 35, 51] all presented experimental evidence of spiral-type coherent structures in a rotating jet. The last three especially were able to single out double spirals using dye visualisation as well as Particle Image Velocimetry. Through loudspeakers, [20] forced the jet at specific azimuthal wavenumbers and observed the resulting flow. In this manner, the robustness of vortex breakdown was established as well as the receptivity of the flow to double or triple spirals.

[50] also performed high fidelity measurements that fitted well with weakly non-parallel spatial stability analysis predictions close to the nozzle at relatively low Reynolds number. [50] found a double spiral co-winding counter-rotating mode present close to the nozzle but decaying faster in the downstream direction than the dominant bending mode. This mode was explained invoking C instabilities.

On the numerical front, [39] used a line vortices model to study the evolution of rotating jets. These calculations brought to light complex interplay between KH phenomena in the axial and azimuthal directions as well as the influence of C effects. These different phenomena are very sensitive to initial conditions, displaying chaotic behaviour. One of the major effects of introducing swirl in the flow is the formation of counter-rotating structures under certain specific initial conditions. These structures can in turn be dispersed by strong KH waves or overtake them. The same authors made multiple contributions on this topic including [40–43], always highlighting the competition between KH and C effects when swirl is introduced in the jet.

[52] describe the fluctuations that arise from a turbulent baseflow taken from LES [57]. Using an eddy-viscosity model, the authors were able to explain the underlying physical mechanisms behind amplification, namely Orr mechanism, LU, and KH. [52] finally provides a mapping to where each phenomenon is expected to dominate throughout the frequency space.

More recently, [45] performed a Large Eddy Simulation (LES) of a swirling flow and then a Spectral Proper Orthogonal Decomposition (SPOD) to obtain the most energetic fluctuations from this flow. This study was performed at relatively low Reynolds number, but attained high swirl, as the focus of the authors was on the description of vortex breakdown. In the regime that is of interest to this study, the authors exhibited four spirals at very low frequency, which were considered to be a spurious consequence of the coordinate system in the publication.

Literature on KH instability dates back to [54] in cylinder flows. It was generalised by [8], where an instability growing simultaneously on radial shear in the axial and azimuthal directions was proposed.

This is the favoured mechanism in [21] for instability growth through local temporal stability analysis of an inviscid swirling jet at high wavenumbers. This approach has the advantage of being purely analytical, which allows a clear separation of the different terms driving instabilities. In turn, this enabled the authors to highlight four separate mechanisms, namely inertial waves, C, axial and azimuthal KH. However, the authors acknowledge that their use of an plug flow profile is known to lead to nonphysical KH solutions.

On the subject of C instabilities, [53] derived what became known as the Rayleigh criterion in the case of parallel flow with no axial component. This criterion states that the existence of a radius where $\partial_r(r^2U_\theta^2) < 0$ is a necessary condition for axisymmetric C instability. In [62], this criterion was found to be sufficient in the case of Couette flows.

A generalised necessary criterion for non axisymmetric instability was further derived in [27]. [31] derived a simpler sufficient criterion for instability in the infinitely large wavenumber limit. [19] proved later that this criterion was linked to C instability by considering a coordinate system turning with the fluid, writing associated inertial effects, and falling back on [31]'s criterion. More recently, further generalisation was performed in [11, 12] for a wider range of profiles and at a higher order. [11, 12, 19, 27, 31, 53, 62] all used generic flow profiles in inviscid local temporal stability analysis. [22, 29, 30, 37, 38, 41] have all conducted local temporal or spatial stability analysis of swirling flows at zero to moderate Reynolds number. These authors all took a prescribed parallel baseflow sometimes as simple as a plug flow then derived dispersion relations analytically or numerically, which can greatly facilitate physical interpretation of obtained modes.

Gallaire et al. [22] identified an absolute instability of double-spiral perturbations in a swirling jet before vortex breakdown. [37] additionally plotted critical curves where the transition from convective to absolute instability takes place depending on co-flow and swirl intensity for every azimuthal wavenumber.

Figure 1: Case layout

In turn, this allowed him to single out the most unstable azimuthal wavenumbers for a given co-flow as the first one transitioning into absolute instability when increasing swirl.

[38] and [30] studied the interplay between swirl and compressibility finding swirl to be more destabilising than compressibility is stabilising. [29] also introduced viscosity and discovered additional types of viscous instabilities. Furthermore, this work compared the modes obtained numerically to experiments and demonstrated satisfying agreement for a range of frequencies.

The different authors cited here disagree on which mode is more unstable when introducing swirl, yet this is not surprising as their base flows also differ. [37] argues in favour of the axisymmetric mode, whereas [22, 29, 30, 38, 41] claim it to be a spiral mode.

The closest study to this one would be [46], who used resolvent analysis on a coaxial swirling jet. The key difference between this work and the present study are geometry and Reynolds number considered. The former is fully turbulent, whereas the latter was decidedly laminar.

This work studies the dynamics of coherent structures in an amplifier-type turbulent swirling jet using resolvent analysis. It is organised as follows: section 2 describes the methodology adopted through the study, beginning with defining the flow configuration in section 2.1. Section 2.2 then presents the procedure followed to obtain the base flow used for this work as well as its main characteristics, and section 2.3 details the theory and implementation of the resolvent analysis framework. Then, section 3 showcases the most important results, namely the gains and the various structures obtained. Finally, section 4 summarises the study.

2 Methodology

2.1 Flow configuration

This study considers an axisymmetric swirling jet emanating from a nozzle into a large domain with a weak non-swirling co-flow, as represented in figure 1. Our cylindrical coordinate system is centred at the nozzle outlet. Using the nozzle radius R as a length scale, the inner wall of the nozzle is given a radius and length of 1. Note that, at its base, the nozzle wall has a small but finite width of $\epsilon = 10^{-4}$, which sharpens to a point at the injection plane.

The flow in this configuration is governed by the dimensionless Navier-Stokes equations,

$$\begin{cases} \underline{\nabla} \cdot \underline{\mathtt{u}} = 0, \\ \partial_t \underline{\mathtt{u}} + \underline{\mathtt{u}} \cdot \underline{\underline{\nabla \mathtt{u}}} + \underline{\nabla} \mathtt{p} - \underline{\nabla} \cdot \left[\left(\underline{\underline{\nabla \mathtt{u}}} + \underline{\underline{\nabla \mathtt{u}}}^T \right) / Re \right] = \underline{0}, \end{cases} \tag{1}$$

where the velocity vector in cylindrical coordinates is $\underline{\mathtt{u}} = \mathtt{u}_x \underline{e}_x + \mathtt{u}_r \underline{e}_r + \mathtt{u}_\theta \underline{e}_\theta$, $\underline{e}_i$ is the unit vector in direction i, and the Reynolds number $Re = U_0 R/\nu_0 = 200,000$ where ν_0 is the reference molecular kinematic viscosity of the fluid and U_0 is the velocity scale.

In this study, the velocity is normalised by setting U_0 equal to the maximum base flow axial velocity at the inlet. Hence, the flow along the inlet inside the nozzle (see figure 1) is prescribed in dimensionless units as,

$$\underline{U}_{inlet}(r) = \tanh\left(6(1-r^2)\right)\left(\underline{e}_x + Sr\underline{e}_\theta\right), \tag{2}$$

where S is the dimensionless swirl intensity. Without loss of generality, this study only considers positive swirl, meaning that fluid particles wind in space in the positive sense defined by the right-hand rule with respect to the axial direction. Inlet profiles are very similar to those presented on figure B3a, and resemble a smooth top-hat profile with a near solid body rotation of dimensionless axial vorticity S. To achieve convergence, it was necessary to introduce a weak axial coflow around the jet, which we specify as,

$$\underline{U}_{coflow}(r) = 2U_m\tilde{r}(1-\tilde{r}/2)\underline{e}_x, \tag{3}$$

with $U_m = 0.05$ and $\tilde{r} = (r-1-\epsilon)/(19-\epsilon)$. Therefore, the axial coflow has a parabolic profile that vanishes along the nozzle wall and increases to about five percent of the jet axial velocity at the radial edge of the computational domain. Regarding the other boundary conditions, no-slip conditions are imposed

along the nozzle walls, symmetry conditions are imposed along the central axis, and stress free boundary conditions are adopted along the outer radial and axial edges. Note that the stress free, also known as zero-traction condition, is a mixed boundary condition involving the pressure and velocity that requires

$$p\underline{n} = \nu \left(\underline{\underline{\nabla u}} + \underline{\underline{\nabla u}}^T \right) \underline{n}, \tag{4}$$

with $\underline{n}$ the vector normal to the boundary – in this case either $\underline{e}_x$ or $\underline{e}_r$.

2.2 Base flow

This paper analyses the coherent structures of a high Reynolds number swirling jet using a linear analysis about the turbulent base flow. For this purpose, a base flow representative of a mean flow, is required as an input. We therefore invoke the concept of the triple decomposition [28], where the velocity and pressure are decomposed into a mean component, a set of spatiotemporally-organised coherent structures, and a background of incoherent turbulent fluctuations. The incoherent fluctuations will be modelled with a turbulence model such that the velocity and pressure may instead be represented as the sum of the base flow and coherent structures, i.e. $\underline{\mathtt{u}} = \underline{U} + \underline{u}$ and $\mathtt{p} = P + p$. Here, the base flow is defined with ensemble averages such that $\overline{\underline{\mathtt{u}}} = \underline{U}$ and $\overline{\mathtt{p}} = P$.

Applying this ensemble averaging framework to equation (1) yields the well-known Reynolds Averaged Navier-Stokes (RANS) equations governing the base flow. Then, invoking a Spalart Allmaras (SA) eddy viscosity model for the Reynolds stress [61], these stationary equations are closed and may be written as,

$$\begin{cases} \underline{\nabla} \cdot \underline{U} = 0, \\ \underline{\underline{\nabla U}} \ \underline{U} + \underline{\nabla} P - \underline{\nabla} \cdot \left[\nu \left(\underline{\underline{\nabla U}} + \underline{\underline{\nabla U}}^T \right) \right] = \underline{0}. \end{cases} \tag{5}$$

Note that, throughout this work, the effective viscosity ν is taken as the sum of the dimensionless molecular viscosity and the eddy viscosity ν_t, i.e. $\nu = 1/Re + \nu_t$.

This setup allows for a base flow with a very thin shear layer, characterised as follows

$$\begin{cases} U_m(x) = \min\limits_r U_x(x,r), \\ r_m(x) = \arg\min\limits_r U_x(x,r), \end{cases} \tag{6}$$

$$\Pi(x,r) = \frac{U_x(x,r) - U_m(x)}{1 - U_m(x)}, \tag{7}$$

$$\Theta(x) = \int_0^{r_m} \Pi(x,r) \left[1 - \Pi(x,r) \right] r \mathrm{d}r. \tag{8}$$

This leads to figure 2 and about $\Theta(R) \approx 0.02$. For reference, the shear layer thickness of the flow used by [57] obtained by LES is also shown, in appropriate non-dimensional units. Thus, the base flow in this study has a very sharp shear layer of finite thickness.

2.2.1 OpenFOAM calculations

All spatial discretisations used in this paper are based on triangular, unstructured, inhomogeneous meshes drawn using `gmsh` [25]. Following a mesh convergence study (see appendix B), the final mesh chosen for this study has about 152,000 nodes.

Equations (5) were solved under the boundary conditions detailed in section 2.1 using the `simpleFoam` solver from the `OpenFOAM` CFD software available at [63]. For the purposes of this code, turbulent eddy viscosity was set to zero at the walls and zero-gradient at all other boundaries.

Base flow calculations were performed over a range of S values from $S = 0$ to $S = 1.6$. This allowed for confirmation that the SA model was able to properly capture the vortex breakdown phenomenon, shown in figure 3, which first appeared in the vicinity of $S = 1.4$. However, since vortex breakdown is well-known to promote self-excited dynamics in swirling jets [15, 44], such large S values will not be considered in the main results. Instead, we will focus on flows with $S \leq 1$. For these S values, it was verified that the system is modally stable, and that the axial velocity on the axis remains positive throughout the domain.

Actual computations were made in parallel using forty 2.10 GHz *Intel(R) Xeon(R) Gold 6230* CPUs with a frequency of 2.10 GHz. Convergence was defined using an absolute tolerance of $\eta = 10^{-12}$ for each calculation. The full configuration is available on GitHub under a GPL-3.0 license.

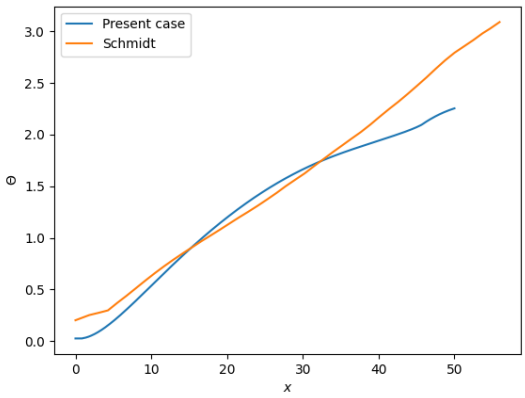

Figure 2: Shear layer thickness Θ of the base flow, compared to the reference case of Schmidt *et al.* [57].

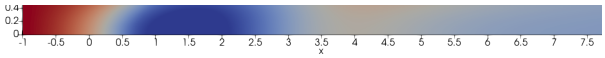

Figure 3: $x-r$ view of the x component of the base flow at $S = 1.6$ close to the nozzle

(a) Axial direction (b) Tangential direction

Figure 4: $x-r$ views of base flow velocities at $S = 1$ close to the nozzle

The result is represented on figure 4 for reference.

2.3 Resolvent analysis

2.3.1 Formalism

Given a base flow, resolvent analysis is a way to model and predict coherent structures of turbulent fluctuations [34, 57, 64]. Said fluctuations $\underline{q} = \left[\underline{u}^T \; p\right]^T$ are three-dimensional and time-dependent but may be Fourier-decomposed into modes with discrete azimuthal wavenumbers m and pulsations ω as

$$\underline{q}(x,r,\theta,t) = \sum_{m=-\infty}^{\infty} \int_0^{\infty} \underline{\hat{q}}_{m,\omega}(x,r) e^{i(m\theta-\omega t)} + \underline{\hat{q}}^*_{m,\omega}(x,r) e^{i(\omega t - m\theta)} \mathrm{d}\omega. \tag{9}$$

In the following, the distinction will be made between a mode observed wrapped in space around $\underline{e}_x$, which is designated to be *winding*, and a mode moving in time around the same axis, which will be called *rotating*. With these conventions, a mode with $m < 0$ is counter-rotating.

Equation (9) makes it clear the desired flow structures are real. This leads to

$$\underline{\hat{q}}_{-m,-\omega} = \underline{\hat{q}}^*_{m,\omega} \tag{10}$$

by unicity of the Fourier decomposition. Thus, $\omega \geq 0$ is imposed with no loss of generality, as in [22].

For the purpose of conciseness, $\underline{\hat{q}}_{m,\omega}$ will simply be written $\underline{q}$ in the following. Using this decomposition leads to the operator replacement $\partial_\theta \leftrightarrow im$ and thus $\underline{\nabla} \leftrightarrow \underline{\nabla}_m$. Hence, the fluctuations equations can be derived

$$\begin{cases} \underline{\nabla}_m \cdot \underline{u} = 0, \\ -i\omega \underline{u} + \underline{\underline{\nabla}_m u} \; \underline{U} + \underline{\underline{\nabla_0 U}} \; \underline{u} + \underline{\nabla}_m p - \underline{\nabla}_m \cdot \left[\nu \left(\underline{\underline{\nabla}_m u} + \underline{\underline{\nabla}_m u}^T \right) \right] = \underline{\nabla}_m \cdot \left(\underline{\overline{u}\overline{u}}^T - \underline{u}\underline{u}^T \right). \end{cases} \tag{11}$$

At this stage, the eddy viscosity is introduced into the perturbation equations in order to improve the accuracy of the linear model, see [13, 47]. This introduction is also consistent with considering equations

(11) as fluctuations of the base flow equations (5), and was performed in several other works such as [1, 48]. Therefore, the viscosity $\nu = 1/Re + \nu_t$ in equation (11) is identical to that used in section 2.2.

The method of resolvent analysis has been detailed in works such as [1, 48, 56, 60] and many others besides, so only a short reminder will be offered here. The core objective of resolvent analysis is to find the right-hand side of equations (11) most amplified by the linear dynamics of the left-hand side, and obtain the associated coherent structures.

Looking at equation (11), the left hand side is linear with respect to the fluctuations but the right side is not. This allows us to write the entire system in matrix form as $\underline{\underline{L}}\,\underline{q} = \underline{\underline{B}}\,\underline{f}$, with

$$\underline{\underline{B}} = \begin{bmatrix} \underline{\underline{0}} \\ \underline{\underline{I}} \end{bmatrix}, \tag{12}$$

so that incompressibility is strictly enforced. Introducing the extractor

$$\underline{\underline{H}} = \begin{bmatrix} \underline{\underline{I}} & \underline{\underline{0}} \end{bmatrix}, \tag{13}$$

one may write $\underline{\underline{H}}\,\underline{q} = \underline{u}$ which in turn gives the resolvent operator $\underline{\underline{R}} = \underline{\underline{H}}\,\underline{\underline{L}}^{-1}\,\underline{\underline{B}}$. This resolvent operator is unique for a given base flow $\underline{Q}$ and a choice of both azimuthal number m and pulsation ω.

From there, it is clear that $\underline{\underline{R}}\,\underline{f} = \underline{u}$. In other words, the resolvent operator links forcing terms with velocity fluctuations in a linear manner. Finally, a Singular Value Decomposition (SVD) of the matrix $\underline{\underline{R}} = \sum_i \sigma^{(i)} \underline{\psi}^{(i)} \underline{\phi}^{(i)H}$ yields the three main quantities of interest:

1. The gains $\sigma^{(i)}$, which can be understood as a ratio of perturbation kinetic energy obtained over non-linear terms work required to produce them. These allow us to order the modes from the most amplified by the linear operator, associated to $\sigma^{(1)}$, to the least amplified.
2. The dominant response mode $\underline{\psi}^{(1)}$ represents the structure which can be expected to arise in the flow fluctuations around the base flow, provided $\sigma^{(1)} \gg 1$ and $\sigma^{(1)} \gg \sigma^{(2)}$.
3. The optimal forcing mode $\underline{\phi}^{(1)}$ gives the normalised least energetic stimulation that will give rise to $\underline{\psi}^{(1)}$ through the linear operator. It is not predictive of flow behaviour, but may still be useful from an engineering perspective to damp a problematic mode.

Resolvent analysis is a linear method of studying instabilities that differs significantly from temporal stability analysis, also known as modal analysis, in three important respects:

1. In the resolvent formalism, the frequency is a parameter, whereas it is an unknown in modal analysis,
2. Response modes obtained through resolvent analysis require their associated forcing in order to exist, whereas temporal eigenmodes are self-sustaining (unstable) or decay (stable),
3. The dominant response mode is expected to collapse onto the first SPOD mode of a real flow in case of strong gain separation and uncoloured turbulent forcing, as established in [9]. Conversely, a normal mode can only be measured in a linearly unstable flow.

It should also be noted that this analysis is global and three-dimensional throughout the domain, which is distinct from the local analyses in the literature of parallel flows. This is a key consideration when studying a spatially-developing flow such as a swirling jet.

2.3.2 Implementation

In order to perform the process detailed in section 2.3.1 around the base flow computed in section 2.2, the Taylor–Hood P2–P1 family and `Basix` elements detailed in [58] were used from the `FEniCSx` finite element library published in [59]. The problem was formulated in weak form in the `UFL` language published in [2] with no special treatment at the axis of symmetry. Interpolation of the base flow between the two codes, `OpenFOAM` and `FEniCSx`, was non trivial and required some smoothing.

In line with section 2.1, the boundary conditions for the fluctuations were set as follows: $\underline{u} = \underline{0}$ for all base flow Dirichlet boundary conditions along the inflow and wall boundaries, stress free at the radial and axial outlet boundaries, and symmetry boundary conditions on the central axis. These symmetry

conditions ensure continuity of the three-dimensional perturbations and are given as

$$\begin{cases} \partial_r u_x = \quad u_r = \quad u_\theta = 0 \text{ if } \ m \ = 0, \\ \quad u_x = \partial_r u_r = \partial_r u_\theta = 0 \text{ if } |m| = 1, \\ \quad u_x = \quad u_r = \quad u_\theta = 0 \text{ else.} \end{cases} \tag{14}$$

Once the system is discretised and projected onto finite elements, the SVD is not computed directly. Indeed there is an equivalence between the SVD of $\underline{\underline{R}}$ and the classic diagonalisation of $\underline{\underline{R}}^H \underline{\underline{W}}_\psi \underline{\underline{R}}$, $\underline{\underline{W}}_\psi$ being the matrix of weights associated with the Hermitian product of response modes $\left\langle \underline{\psi}^{(i)}, \underline{\psi}^{(j)} \right\rangle_\psi = \underline{\psi}^{(i)} \underline{\underline{W}}_\psi \underline{\psi}^{(j)H} = \delta^i_j$. This gives

$$\underline{\underline{R}} = \sum_i \sigma^{(i)} \underline{\psi}^{(i)} \underline{\phi}^{(i)H} \Leftrightarrow \underline{\underline{R}}^H \underline{\underline{W}}_\psi \underline{\underline{R}} = \sum_i \sigma^{(i)2} \underline{\phi}^{(i)} \underline{\phi}^{(i)H}. \tag{15}$$

This allows for the formulation of an eigenvalue problem for the leading eigenpair

$$\sigma^{(1)2} = \max_{\underline{\phi}} \frac{\underline{\phi}^H \underline{\underline{R}}^H \underline{\underline{W}}_\psi \underline{\underline{R}} \underline{\phi}}{\underline{\phi}^H \underline{\underline{W}}_\phi \underline{\phi}}, \qquad \underline{\phi}^{(1)} = \arg\max_{\underline{\phi}} \frac{\underline{\phi}^H \underline{\underline{R}}^H \underline{\underline{W}}_\psi \underline{\underline{R}} \underline{\phi}}{\underline{\phi}^H \underline{\underline{W}}_\phi \underline{\phi}}. \tag{16}$$

This formulation handles the specificity of cylindrical coordinates in the mass matrices $\underline{\underline{W}}_\psi$ and $\underline{\underline{W}}_\phi$ as well as inside the operator $\underline{\nabla}_m$.

Weights can also be introduced in matrices $\underline{\underline{B}}$ and $\underline{\underline{W}}_\psi$. Having $\underline{\underline{B}}$ go to zero in a region in space is equivalent to preventing this region from being forced in relations (11). Since that region is still accounted for in $\underline{\underline{W}}_\phi$, this leads to a range of the forcing vector $\underline{\phi}$ that has no influence in the numerator of equation (16), but increases the denominator. Therefore, the eigenvalue solver will always set the forcing in that region to zero.

Similarly, having $\underline{\underline{W}}_\psi$ go to zero for a region in space prevents response from affecting the numerator of equation (16), removing any incentive for forcing that would lead to structures there. $\underline{\psi}$ and $\underline{\phi}$ live in identical spaces, so the only added value of considering different weighting matrices $\underline{\underline{W}}_\psi$ and $\underline{\underline{W}}_\phi$ is this option of constraining response modes.

In the following, $\underline{\underline{B}}$ was forced to zero for the top left of the domain to prevent spurious forcing exploiting base flow interpolation defects in the radial far field. In other words, forcing was constrained to the lower part of the domain for numerical reasons.

The `FEniCSx` library alone proved insufficient to perform the eigenvalue calculations required by the resolvent method detailed in section 2.3.1. Thus the `PETSc` library of [5–7] was used. The parallel version of this library developed in [65] was especially useful. `PETSc` was accessed through the `petsc4py` package published in [14].

In practice the factorization of the $\underline{\underline{L}}$ operator was performed using MUMPS [3, 4] and the eigenvalues were retrieved using the Krylov-Schur solver implemented in SLEPc, see [26, 55]. Computations were run on thirty-five *Intel(R) Xeon(R) Gold 6240Y* CPUs running at 2.60 GHz with a consistent absolute tolerance of $\eta = 10^{-12}$. The complete code is available on GitHub under a GPL-3.0 license.

3 Results

3.1 Flow behaviour with increasing swirl

Figure 5 represent the evolution of the dominant gains $\sigma^{(1)}$ as a function of Strouhal number $St = \omega R/\pi U$ for different azimuthal wavenumbers m. Each plot was made for a different swirl intensity S.

As expected, introducing swirl breaks axisymmetry in equations (11). Hence, perturbation equations are no longer invariant with respect to the transformation $\theta \leftrightarrow -\theta$. Therefore, curves of constant $|m|$ no longer collapse on each other. Recall relation (10) which leads to

$$\forall m \in \mathbb{N}, \forall S \in \mathbb{R}, \lim_{St \to 0^+} \sigma^{(i)}_m \Big|_S = \lim_{St \to 0^+} \sigma^{(i)}_{-m} \Big|_S. \tag{17}$$

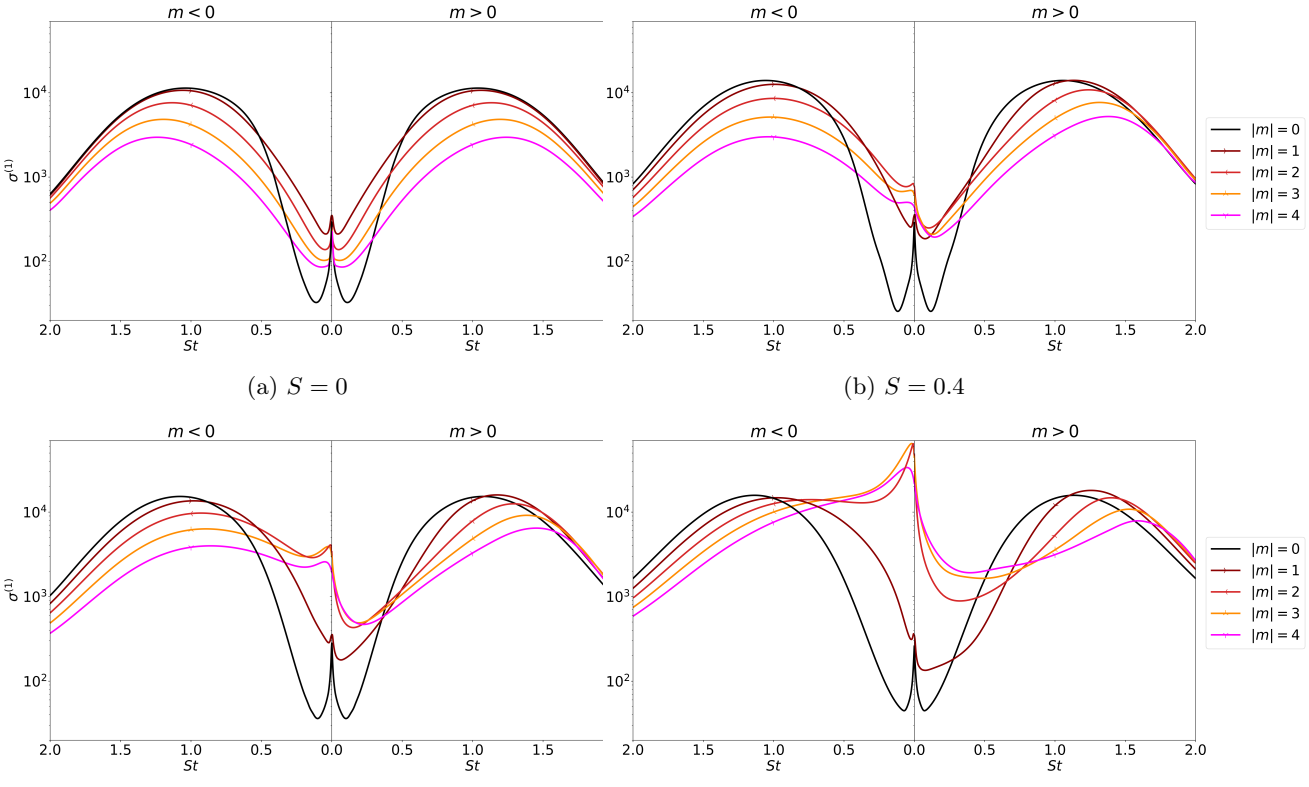

(a) $S = 0$ (b) $S = 0.4$

(c) $S = 0.6$ (d) $S = 1$

Figure 5: Gains as a function of Strouhal number for different values of S and m

and this behaviour is readily visible on figure 5. Also note that the gains generally become more damped as $|m|$ increases, which may be attributed to viscous damping acting on smaller-scale structures.

The implementation chosen in section 2.3.2 allows for exploration of very low Strouhal numbers, where strong amplification is observed at high swirl. Because of the boundary conditions detailed in 2.1, increasing S amounts to increasing U_θ while keeping U_x constant at the nozzle inlet. Hence, a higher swirl intensity means that the base flow has more kinetic energy and stronger shear, both of which may be leveraged by perturbations to achieve increased amplification at higher S values.

However, comparing $S = 0$ to $S = 1$, the base flow structure is very similar, the base flow kinetic energy has less than doubled by introducing swirl, and the strength of the additional azimuthal shear component $\partial_r U_\theta$ at $S = 1$ is roughly equivalent to the axial shear $\partial_r U_x$ already present at $S = 0$. Yet figure 5 indicates that this change in S causes a gain increase of almost two orders of magnitude. Therefore, the dependence of $\sigma^{(1)}$ on swirl intensity is highly nonlinear at low frequencies. Hence, it seems likely that a new amplification mechanism absent in non-swirling jets comes into play as swirl is increased. This idea will be investigated further below.

3.1.1 Influence of swirl on the $m = 0$ and $m = \pm 1$ modes

First of all, the axisymmetric behaviour does not substantially change with S. KH modes at $m = 0$ dominate flow behaviour for frequencies $St > 0.5$ in the absence of swirl on figure 5a. This is expected, as $m = 0$ leads to the highest gains for pure $\partial_r U_x$ shear in two dimensions as established in [16] by local temporal stability analysis. When swirl is introduced, the $m = 0$ curve and associated structures become overtaken by other azimuthal wavenumbers $m > 0$ at high frequencies $St > 1$.

This could be because KH instabilities as described in [21] again in a local temporal stability framework are growing along flow streamlines. A $m = 0$ mode is invariant along the $\underline{e}_\theta$ direction and incapable of evolving azimuthally along streamlines tilted by the presence of U_θ. Therefore, it is impossible for a linear axisymmetric perturbation to leverage azimuthal KH, no matter the frequency regime. Hence,

we suggest that the optimal gains for the nonaxisymmetric modes overtake the optimal gain of the axisymmetric mode in the swirling regime at high frequencies because nonzero wavenumbers are able to leverage azimuthal KH for energy transfer and thus become more amplified.

The gains of the bending modes $|m| = 1$ separate for non-zero swirl as all $|m| > 0$ modes do, but these apparently do not undergo radical change as S increases. Figure 5 seems to imply a phenomenon not unlike Doppler shift, with a $m = 1$ curve shifting into the high frequencies, and the $m = -1$ curve into the low frequencies with a slight additional amplification relative to overall swirl intensity.

Some modal analyses instead highlight increasing amplification of axisymmetric and spiral modes with swirl. [37] find that the $m = 0$ mode is the most amplified in their local analysis. [29–31, 50] all compute the $m = -1$ mode taking over the axisymmetric KH mode as swirl increases and eventually leading the way to instability for a swirling jet.

Finally, [17, 21] both argue that an infinite wavenumber has optimal gain as swirl increases, though the former also concedes this is probably due to the choice of an infinitely thin shear layer.

Recall from section 1 that all the authors above perform local temporal stability analysis, which includes a parallel flow assumption. The formalism of [50] is also based on local spatial stability analysis, but only weakly non-parallel. As stated in 2.3.1, there are significant differences between this approach and the one pursued here, which could explain the disparity between results.

The 'rebound' of gains around $St = 0$ on figure 5 for the axisymmetric mode that persists for different values of S is apparently associated with an interaction of the computed response with the nozzle wall. This will be discussed further in section 3.3.

3.1.2 Influence of swirl on the $|m| > 1$ modes

Figure 5 features a spectacular amplification of modes with $|m| > 1$ at low Strouhal numbers, especially for $m < -1$. Indeed, the gains obtained in this regime become even larger than the maximum of the axisymmetric mode at $St \approx 1$ traditionally associated with KH waves. The phenomenon persists up to the highest wavenumber studied $|m| = 5$, but wears off around $St \approx 1$.

Even before looking at the mode structure in detail, this increased amplification of low St $|m| > 1$ modes points to the LU mechanism as detailed in [49, 52] in a resolvent formalism. This phenomenon, which exploits shear to create streaks, is expected to play an important role in flow physics for $|m| > 1$ and low St according to the mechanism map of [52].

This amplification discrepancy is even more dramatic and longer lasting for $m < 0$, or counter-rotating modes. This is not a new result. A regime of swirl intensity where such modes are amplified has already been seen by [22, 29, 32, 33, 36, 38, 50]. Authors present different results when quantifying growth rates, but the simple persistence of counter-rotating modes for the variety of base flows considered, from the Batchelor vortex to experimentally-fitted profiles, does suggest some degree of generality. Of course, the differences between the local temporal stability analysis results of these works and the global resolvent analysis outlined in section 2.3.1 still apply.

Similar preference for $m < 0$ can also be found in the resolvent analysis conducted by [46] for a coaxial jet, whose gain curves on their figure 10 bear striking resemblance to figure 5. The study by Montagnani *et al.* is very similar to the current case, though it was performed at a significantly lower Reynolds number, and for a co-axial jet.

Finally, experimental evidence of a double spiral in a swirling turbulent jet can be found in [10, 20, 22, 35, 50], where double spiral counter-rotating co-winding structures plays a key role, especially around conical vortex breakdown. These structures were extracted from the flows through a variety of techniques from hot wire probes to dye visualisations.

3.1.3 Low rank behaviour

For reduced order modelling, it is desirable to have a large gain separation $\sigma^{(1)} \gg \sigma^{(2)}$ for each m over a wide range of St, as established in [9]. Figure 6 shows large gain separation throughout the range of Strouhal numbers considered for $m = -2$, and this behaviour is representative of the gain separation for all m at similar S values. It is remarkable that this separation remains large at low frequencies, as straight (non-swirling) jets exhibit less gain separation, and, thus, higher-rank behaviour, at low St as seen in [57].

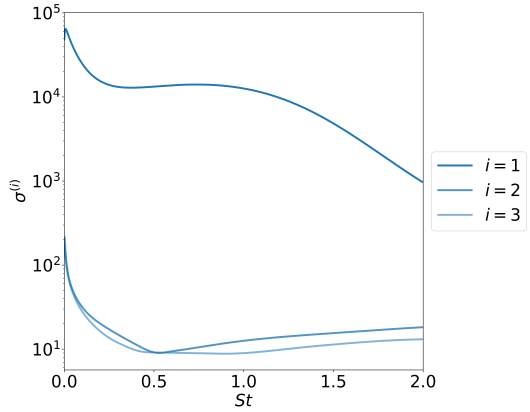

Figure 6: Three first gains as a function of Strouhal number for $(S, m) = (1, -2)$

(a) $m = -2$ (b) $m = 2$

Figure 7: 3D isocontours at 10% for $(S, St) = (1, 0.004), m \in \{-2, 2\}$. Axial forcing $\phi_x^{(1)}$ is in cyan-yellow, response $\psi_x^{(1)}$ in blue-red. The black arrows represent main baseflow velocity components, the nozzle is in transparent black.

As established in [9], the optimal response mode $\underline{\psi}^{(1)}$ is the best single rank approximation of fluctuation energy. Because of the large gain separation observed, it is reasonable to represent energetically significant dynamics around the base flow using only a single mode pair $\underline{\phi}^{(1)}$ and $\underline{\psi}^{(1)}$ for every m and St, which is equivalent to reduced order modelling of the flow.

3.2 Most amplified modes

The focus of our study naturally lands on the most amplified response mode, located at $(S, m, St) = (1, -2, 0.004)$, the highest peak of figure 5d. This 3D co-rotating mode is depicted in figure 7a alongside its oppositely-rotating $m = 2$ counterpart. For each, isosurfaces of axial forcing and of velocity response are shown at 10% of their respective maximum values.

From figure 7a, it is apparent that both double-spiral modes wind in the same direction in space, despite rotating in opposite directions. Nonetheless, the modes wind with a very different pitch. They bear close resemblance to modes exhibited in [15], more specifically figure 11 and 12, which present co-rotating $|m| = 1$ and counter-rotating $|m| = 2$ structures respectively. Interestingly, these structures persist in this study at much higher swirl and exhibit the same basic features as figure 7. Douglas *et al.* [15] computed these modes using global temporal stability analysis and numerical continuation at a much higher swirl number than $S = 1$ considered here, which could be an indication that these structures are self-sustaining.

3.2.1 The role of the lift-up mechanism

The forcing for $|m| = 2$ is extremely localised to the nozzle lip and very similar in appearance. Wrapped around the nozzle, it acts in the region with the highest axial and azimuthal shear. The forcing mode envelope ends at $x \approx 0$ whereas the response picks up from $x \approx 4$ onward.

Therefore, extremely localised forcing at the nozzle produces a very large downstream response. The lack of any significant overlap between the forcing and response modes is a characteristic of convective instabilities captured by resolvent analysis. The absence of overlap also points to a non-modal amplification mechanism linked to the non-normality of the linear operator that can not be accurately reproduced by local temporal stability analysis.

At this point, a closer look was taken at specific amplification mechanisms. The sensitivity analysis performed in [52] was considered inapplicable here. Even though this concept was developed for the study

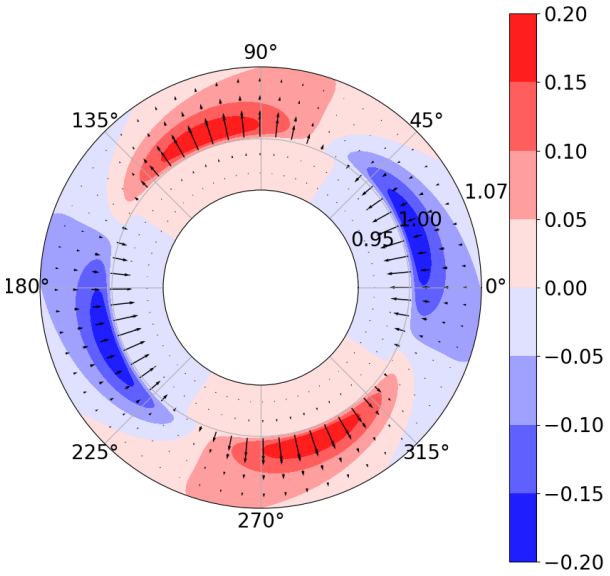

Figure 8: Cross plane of the forcing $\underline{\phi}^{(1)}$ at $x = 0$ around the nozzle for $(S, m, St) = (1, -2, 0.004)$. Contours are axial response $\psi_x^{(1)}$.

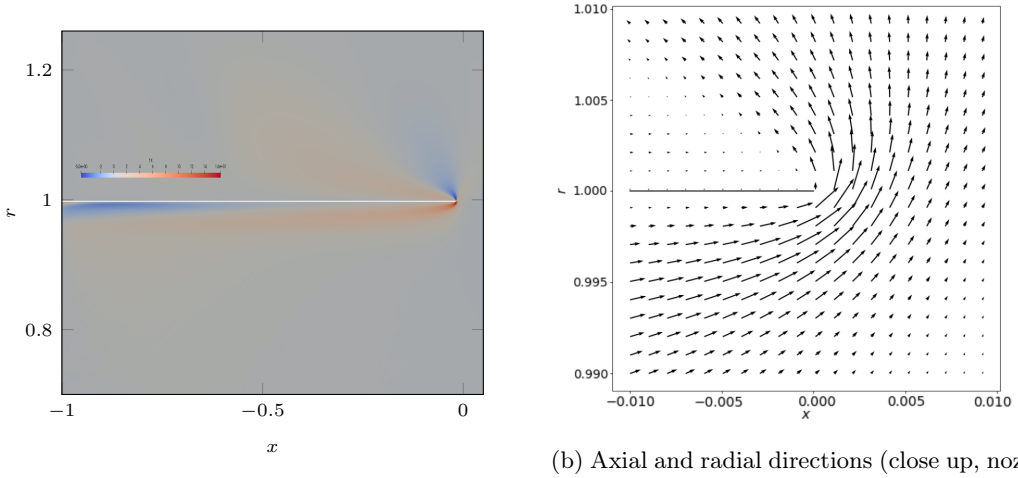

(a) Axial direction, nozzle in white

(b) Axial and radial directions (close up, nozzle in black)

Figure 9: Forcing $\underline{\phi}^{(1)}$ at the nozzle for $(S, m, St) = (1, -2, 0.004)$.

of turbulent jets with resolvent analysis, the introduction of a wall gives strong incentive for the optimal forcing to exist close to the wall where shear is strongest, and for the optimal response to evolve far from it, where it has room to grow and expand via convective instability. This leads to marked spatial separation of forcing and response for much of the parameter space, and the sensitivity analysis presented in [52] was expected to produce little insight here.

Separation between the locations of forcing and response is also a defining trait of the LU phenomenon, where forcing leads to streak formation further downstream in the flow. Figure 8 shows a slice of the forcing vectors superposed over contours of the axial response. As expected, the forcing $\underline{\phi}$ is found to pick up fast-moving fluid from inside the nozzle $r < 1$ and 'lift' it up. This fast moving flow induces strong axial velocity fluctuations, as visible in figure 8. In contrast to the usual LU mechanics in the flow over a flat plate established in [18], there are no prominent 'roll' vortex structures visible in our results.

The presence of LU can be further investigated by studying the forcing at the nozzle in detail. On figure 9 one can see forcing structures tightly wrapped around the nozzle, especially focused at its tip, leading to a clear LU effect where the gradients of the base flow are strongest. The presence of LU and streaks in non-swirling jets was established in [49] using both experimental data and the resolvent method. LU was also listed as a dominant mechanism at low frequency for all $|m| > 1$ in [52] also using resolvent analysis. Therefore, the presence of the same LU mechanism in a swirling jet at low frequencies is expected, at least for small swirl. It seems to persist all the way to $S = 1$.

This explains why $|m| = 1$ or $m = 0$ modes appear less amplified than higher $|m|$ modes at low frequency on figure 5. Indeed, an $m = 0$ incompressible mode cannot generate a streak, and a $|m| = 1$ streak breaks base flow axisymmetry, preventing it from growing. Therefore, we find it unlikely that these modes are produced predominantly by the LU mechanism.

Indeed, looking back on figure 7b, the $m = 2$ mode bears close resemble to a pure streak, as in figure 5 of [52] or figure 9 of [49], who both find streaks in straight jets using resolvent analysis. However, the presence of LU does not explain why modes with $m < 0$ are so much more favoured over $m > 0$ ones, or the presence of a such a marked frequency peak at very low frequency.

3.2.2 About other amplification mechanisms

The tilted structure of the optimal forcing below and above the nozzle visible on figure 9a is suggestive of the Orr amplification mechanism. This mechanism causes amplification by allowing a structure tilted against the base shear to leverage its straightening by the flow's shear such that it grows in a transient manner. According to [52], this phenomenon is also significant at low frequency, particularly for $m = 0$ modes.

In this study, amplification by the Orr mechanism is expected to be present across the parameter space, but observed dominating only in a restricted regime of axisymmetric modes at low frequency. The forcing mode displayed on figure 9a is noticeably more tilted than in [52] where its angle to the mean shear was about 45°. This can be related to the significantly thinner shear layer of the current case as illustrated in section 2.1.

'Pure' Orr-type modes are also expected to have a response which changes tilting orientation along x as in [24, 34]. The latter study uses resolvent analysis to delve into the details of the Orr mechanism, notably characterising it as a non-modal phenomenon that temporal stability analysis therefore cannot capture. The most amplified mode visible on figure 7 does not display the main trait associated with a 'pure' Orr response, namely tilted structures straightening as x increases.

[36] mentions interactions between inertial waves and KH modes as a phenomenon that could occur at low frequencies in parallel jet-type swirling flows. In such circumstances, this interaction has a stabilising effect on $m > 0$ modes. It is well possible that long-range feedback through inertial waves may play a role in our results, but it is not obvious at this point how such effects could be rigorously identified.

KH instabilities may also explain the enormous gain values observed in figure 5. It is easier to think about KH instabilities in the context of a parallel flow. Writing $\underline{U} = U_x(r)\underline{e}_x + U_\theta(r)\underline{e}_\theta$ and periodicity, it becomes possible to write

$$\underline{q}(x, r, \theta, t) = \sum_{m=-\infty}^{\infty} \int_{-\infty}^{\infty} \int_{-\infty}^{\infty} \underline{\hat{q}}_{k,m,\omega}(r) e^{i(kx+m\theta-\omega t)} + \underline{\hat{q}}^*_{k,m,\omega}(r) e^{i(\omega t-m\theta-kx)} \mathrm{d}k\mathrm{d}\omega. \tag{18}$$

instead of equation (9). One can then define a wavevector $\underline{\Lambda} = k\underline{e}_x + m\underline{e}_\theta$ for the fluctuations and a principal shear vector $\underline{\Sigma} = \partial_r U_x \underline{e}_x + \partial_r(U_\theta/r)\underline{e}_\theta$ for the base flow.

In this simplified context, consider a cylinder of constant radius r. It is possible to see this cylinder as the interface between two fluids of velocity $\underline{U}(r^-)$ and $\underline{U}(r^+)$. Instabilities on this surface may be studied in the $\underline{U} - \underline{e}_r$ plane. Neglecting curvature, one recovers the result of [21] extrapolated from [16] that the instability growth rate of the KH instability on the cylinder surface scales as $\underline{\Lambda} \cdot \underline{\Sigma}$.

This scalar product may also be derived directly from the phase of the fluctuations along base flow streamlines

$$\vartheta = kx + m\theta - \omega t. \tag{19}$$

By itself, the phase is not informative of fluctuations' behaviour. Taking the derivative of relation (19) with respect to time yields the Doppler-shifted frequency

$$\gamma = kU_x + m\frac{U_\theta}{r} - \omega. \tag{20}$$

This quantity appears in [11, 12, 27, 31] and $i\gamma$ is called Doppler-shifted growth rate in [11] for a complex ω. Taking its derivative in the radial direction gives

$$\partial_r\gamma = k\partial_r U_x + m\partial_r\left(\frac{U_\theta}{r}\right) \Rightarrow \partial_r\gamma = \underline{\Lambda}\cdot\underline{\Sigma}. \tag{21}$$

It is proposed to use the dot criterion $\underline{\Lambda}\cdot\underline{\Sigma}$ as an indicator of the presence of shear instability. Coincidentally, this product is also relevant to C instabilities. The existence of an r_0 so that $\underline{\Lambda}\cdot\underline{\Sigma}(r_0) = 0$ is a sufficient condition for C instability in [31, equation (5.6)].

Although limited to the large wavenumber limit, this result appears again in [22], where it is also argued that for a viscous swirling jet with weak co-flow an $m = -2$ spiral is expected to become absolutely unstable first. Its derivation in that work involves a Doppler-shifted frequency and looking for a stationary wave in the regime $\|\underline{\Lambda}\| \gg 1$. The same product appears again at leading order in the Wentzel-Kramers-Brillouin (WKB) analysis of [11] also in the large wavenumber approximation (equation (3.8)). At first order, it would appear that the two mechanisms of KH and C work against each other.

However, for a pure LU mode, we also expect to have $\underline{\Lambda}\cdot\underline{\Sigma} = 0$. Indeed, considering a non-swirling flow where $\underline{\Sigma} = \partial_r U_x \underline{e}_x$, and an idealised response made purely of very long streaks. The existence of LU means $|m| > 0$ and very long streaks mean $k \to 0$ which also leads to $\underline{\Lambda}\cdot\underline{\Sigma}$. Therefore, there is no equivalence between a zero dot criterion and a C instability. Indeed, it is only a sufficient condition for its presence.

Of course, the method presented in section 2.3 is not local. So in order to exploit the dot criterion k must be approximated. Here, this is done using

$$k \approx \Re\left(\frac{\partial_x u_x}{i u_x}\right). \tag{22}$$

The dot criterion exhibited in equation (21) was computed and averaged over the envelope of the modes. This envelope was defined as the area where the square of mode amplitude $\|\underline{u}\|^2 = |u_x|^2 + |u_r|^2 + |u_\theta|^2$ was above ten percent of its maximum value. Taking this region as $\mathcal{A}$ and its surface area as $A(\mathcal{A})$, the quantity of interest becomes mode alignment

$$\chi = \frac{1}{A(\mathcal{A})}\int_{\mathcal{A}} \frac{\underline{\Lambda}\cdot\underline{\Sigma}}{\|\underline{\Lambda}\|\,\|\underline{\Sigma}\|}\mathrm{d}A. \tag{23}$$

In the case $(S, m, St) = (1, -2, 0.004)$, $\chi \approx 10^{-3}$. Based on this very small alignment with base shear, we conclude that the observed dramatic amplification at low Strouhal numbers is not a KH instability, but that it could be a C one.

χ is visible on figure 10 for a broader range of the parameter space. Overall, the alignment increases with St. This increase is expected as KH becomes the dominant mechanism for driving instability at high frequency. Conversely, χ remains low in a narrow regime around zero frequency, which is the region where lift-up is expected, and C could exist. This region of low alignment seems to narrow sharply as swirl intensity S increases. Likewise, gains around $St = 0$ on figure 5 peak for a narrow range of frequencies as S increases.

Evolution of alignment relative to S is pretty straightforward in the $m = 2$ case, with region of low alignment growing with swirl. Behaviour for $m = -2$ is less intuitive, with KH instabilities quite quickly taking over all the way to $St \approx 0.75$ up to $S \approx 4$. At higher S, there seems to be a valley forming, with KH receding in the high frequency, high swirl regime. This is the only region where the previous observation that χ increases with St is shown wrong.

This pattern is consistent with the gains on figure 5 when associating variations of χ and $\sigma^{(1)}$. Extremes of alignment correspond to a perturbation that could be understood as making the most of

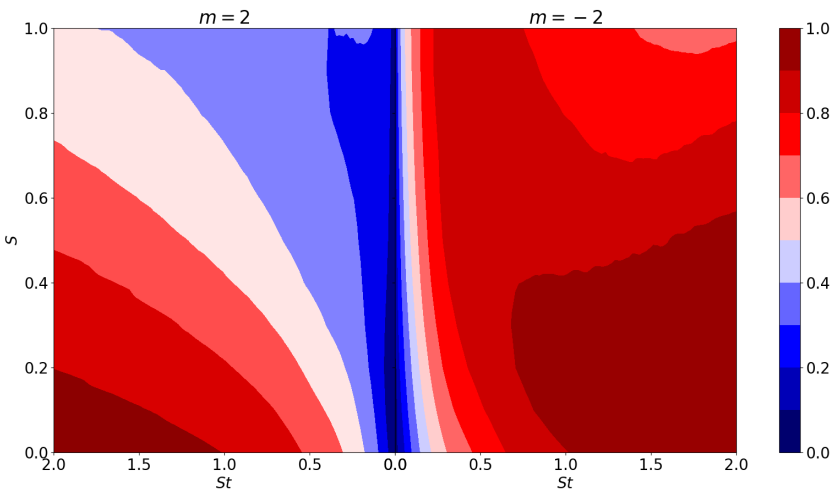

Figure 10: Contour of averaged wavenumber-principal shear relative alignment χ as a function of swirl intensity S and Strouhal number St for $m \in \{-2, 2\}$.

(a) No constrain

(b) Response constrained to $x > 1$

Figure 11: Axial component of the response $\psi_x^{(1)}$ for $(S, m, St) = (0, 2, 0)$

the C or KH amplification mechanism, and show on the gain curves as peaks. Indeed the peak around $St \approx 1$ visible on figure 5d for $m = -2$ traditionally associated to KH seems to shift towards $St \approx 0.5$ as S increases, which is also the case on the alignment map.

Therefore, even if the magnitude of χ does not directly translate into a gain, it teaches us something about their structure and the mechanism leveraged. Hence, obtaining the most amplified mode throughout the parameter space $(S, m, St) = (1, -2, 0.004)$ at an alignment minimum is consistent with the relevance of χ as a mechanism discriminator, and with the witnessed amplification not being a KH instability.

3.3 Outer mode

Another point in the parameter space worthy of attention is the low end of figure 5a for $|m| > 1$. The choice of $m = 2$ makes for easier comparison with the modes of section 3.2. Isocontours of this mode are displayed on figure 11a.

3.3.1 Shear outside the nozzle

The response is strongly concentrated on the radial exterior of the nozzle, latched onto a region of slow moving fluid. It is not allowed to wind or rotate because of the parameter $St = 0$ – it has to remain steady. This behaviour persists for all S. This is a new result - previous calculations comparable to this one such as [46, 52] did not include a nozzle inside the computational domain and thus could not observe these dynamics.

It turns out that the base flow located radially outside of the nozzle is subject to gradients that are about ten times less intense than those inside the nozzle, see figure 12a. It seems these gradients close to the wall are not entirely generated by the coflow but rather by the significant entrainment induced by the jet visible on the streamlines of figure 12b. This contraction leads to a rapid radial increase in axial velocity radially-outside of the nozzle, and therefore strong shear. Indeed, there is evidence of LU in the forcing structure on the outer edge of the nozzle, see figure 13, with vectors roughly orthogonal to the baseflow streamlines visible on figure 12a.

In the end, the overall slower pace of convection on the outside of the nozzle could also play to the advantage of LU, since forcing mechanisms there have more time to "build-up" streaks before they get

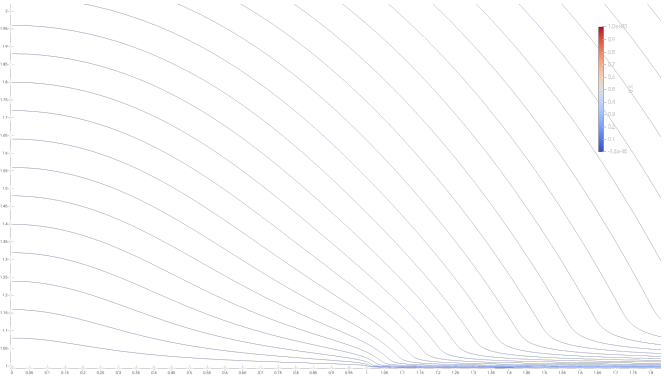

(a) Baseflow velocity norm at $x = -0.01$ (b) Streamlines

Figure 12: Baseflow visualisations on top of the nozzle

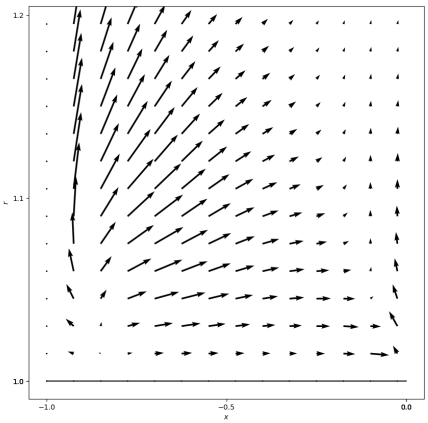

Figure 13: Forcing vectors $\left[\phi_x^{(1)}\ \phi_r^{(1)}\right]^T$ atop the nozzle for $(S, m, St) = (0, 2, 0)$.

advected away in comparison to structures inside the nozzle. Note that contrary to the structures studied in section 3.2, here the forcing and response modes are co-located.

This phenomenon also explains the "rebound" of axisymmetric gain curves around $St = 0$ regardless of swirl intensity observed on figure 5. Since structures in this regime appear fixed on top of the nozzle where they are able to leverage KH, they are unaffected by swirl inside it.

3.3.2 Spread-out streaks

Another clearly visible feature of this mode are the streaks created in the shear layer. Figure 11a presents a response concentrated on top of the nozzle, but also a diffuse, weak component of the response that exists throughout most of the shear layer. This should not be a surprise, as the LU mechanism detailed in section 3.3.1 is known to produce streaks. These structures are expected to be formed on top of the nozzle, but manifest downstream. In this process, the streaks are spread over the whole shear layer.

In order to measure the importance of these streaks in the final gain, the response mass matrix $\underline{\underline{W}}_q$ of equation (16) was weighted to only consider response in the region $x > 1$ and an extra resolvent calculation was performed for the same parameters. This process yields figure 11b, which is very similar to 11a.

Therefore, the streaks generated downstream are energetic – or simply spread out – enough to secure the most amplified position on their own, overtaking other structures without the need for the energy located around the nozzle. Moreover, the structure external to the nozzle is damped but not fully removed after the penalisation. This is significant because by relation (16), such a structure does not directly

contribute to the gain yet still costs energy to produce. It seems that the outer structure is essential to the creation of the streaks, otherwise it would not have survived the weighting process.

The modes only tell part of the story. Between the two modes on figure 11, who are associated to different operators, there is a gain variation of about sixteen percent. Thus, the smeared streaks play a significant role in the overall gain even if at any given point in the shear layer their amplitude do not compare to the outer nozzle structures.

4 Conclusion

This study presented a resolvent analysis of a turbulent swirling jet. In section 2.2, the computation process for the base flow and its associated eddy viscosity was detailed. The use of an open source solver proved critical to achieve the desired Reynolds number of $Re = 200,000$. Section 2.3 briefly reviewed the theory behind the resolvent analysis method and its implementation for this study. The latter is available online via the lead author's private repository.

The method yielded two significant results. Firstly, strong gain separation and significant amplification of low frequency structures were noted in section 3.1 as swirl increased, which was explained by a detailed study of the most amplified mode in section 3.2. The associated coherent structure was very large, taking almost all the shear layer, and manifested some distance away from the nozzle. This double spiral co-winding counter-rotating mode is amplified by a combination of the lift-up mechanism, the Orr mechanism, and a strong centrifugal mechanism. As a response mode, this structure cannot arise or survive without sustained forcing at the nozzle.

A criterion based on relative alignment of perturbation wavenumber and principal shear direction was presented to discriminate between Kelvin-Helmholtz and centrifugal instability mechanisms. This criterion shed a new light on the gains exhibited in section 3.1 by allowing for easier isolation of regimes where shear or centrifugal instabilities dominates. Furthermore, the co-winding nature of the most amplified mode was justified by this criterion, naturally explaining the larger amplification for counter-rotating modes as a consequence of advection.

The second result of import coming from the resolvent analysis of the turbulent swirling jet considered comes from the choice to include a finite height nozzle inside the computational domain. This leads at zero frequency and in the absence of swirl to a most peculiar behaviour studied in section 3.3. This structure latched outside the nozzle, using entrainment as a source of shear to produce streaks that extend throughout the shear layer from the nozzle tip. Contribution of these streaks to gain was shown to be significant.

Amongst the drawbacks of the proposed approach, how much the choice of the Spalart-Allmaras eddy viscosity model in section 2.2 influenced the final result remains unknown. Its inclusion in the fluctuations has been shown to improve performance relative to its absence in many cases, but such improvement is not theoretically guaranteed.

Future work on the subject could try to reproduce behaviours presented here by experimental or numerical means other than local temporal stability analysis. The interplay between Kelvin-Helmholtz and centrifugal instabilities could be explored in more detail, as the influence of inertial waves. A sensitivity analysis, or a more detailed modal one, could prove useful in differentiating the mechanisms at play here.

Declarations

The authors declare no conflict of interest relative to this work.

Appendix A Validation case

In this section results from the developed code will be compared to known publications. The emphasis here is therefore proving the validity of design choices outlined in sections 2.1, 2.2.1 and 2.3.2, not introducing new phenomena. To increase confidence in our model, reproductions of figure 3.(a) and 7.(a) of [44], as well as figure 6.6 from [23] were made. They will not be discussed here for the sake of brevity.

The case considered instead is closer to the one described in section 2.1, namely the non-swirling jet based on [52]. To better compare with the reference, the nozzle was cut out and calculations performed on $x \in [0; 49]$. Figure A1 is to be compared with figure 4(b) of that work. This graph differs notably from

its reference - gains are lower than expected, the peak of the $m = 0$ curve happens at a higher frequency, and the other curves have a marked increase before the expected monotonic decrease.

However, there are several points where our model substantially differs from the reference :

- Base flows come from different methods - one is the result of a LES calculation, the other a RANS process,
- Eddy viscosity models also differ, one being a length scale model and the other being the SA model - even though qualitatively similar, they vary by about a factor three.

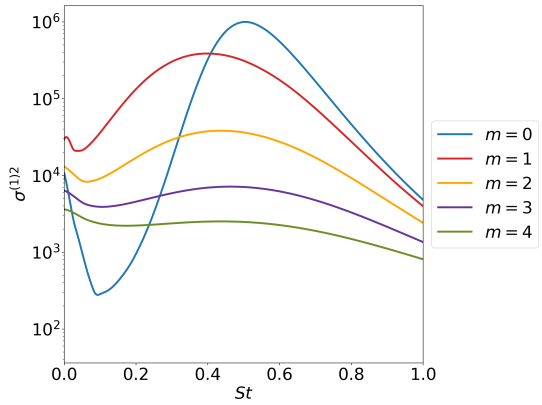

Figure A1: Squared gains as a function of Strouhal number for a variety of azimuthal wavenumbers with no nozzle

A qualitative comparison of response and forcing modes was also done on figure A2, which is to be compared to figures 9(b) and (c) of [52]. These structures are qualitatively very close to the reference, though somewhat shorter. This is probably due to a difference in the eddy viscosity used, which leads to different localised damping. It can be observed that the eddy viscosity used in this study steadily increases with x whereas that of [52] peaks and eventually decays.

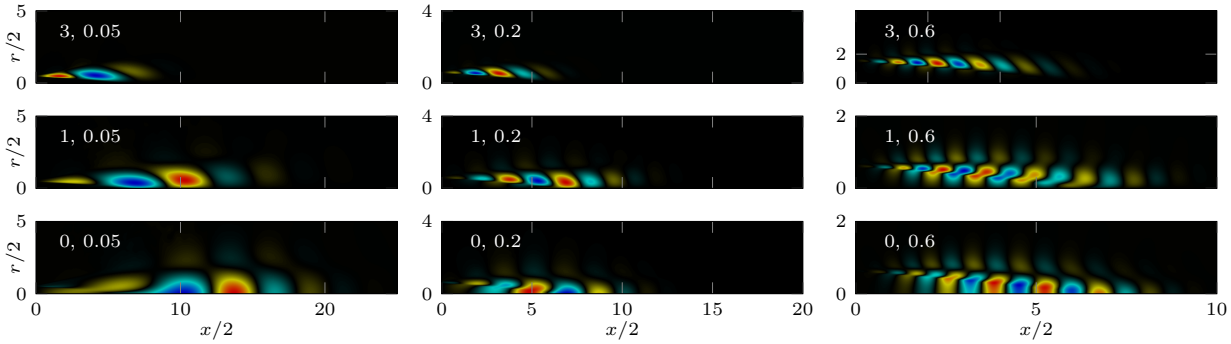

(a) Resolvent response

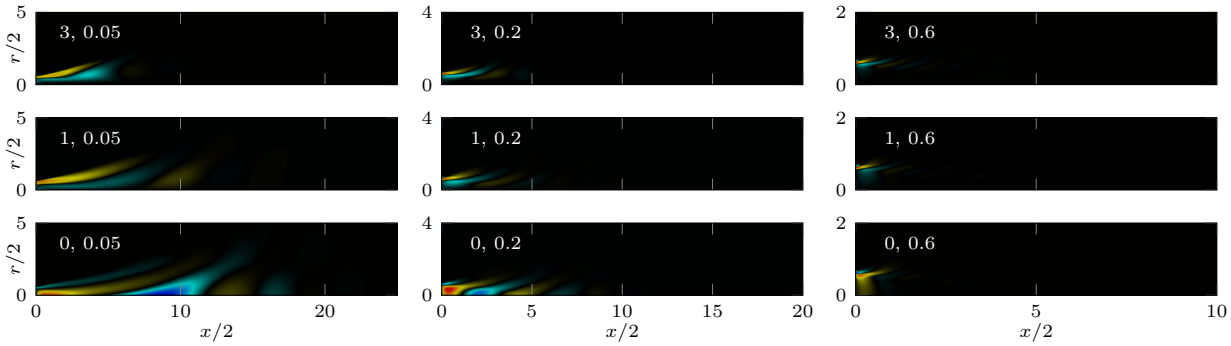

(b) Resolvent forcing

Figure A2: Resolvent modes for $(m, St) \in \{0, 1, 3\} \times \{0.05, 0.2, 0.6\}$. Scaling is adjusted to facilitate comparaison to [52]

Appendix B Mesh refinement

As part of the validation process of the code used in this work, convergence with respect to mesh refinement was verified. In the usual manner, a very refined mesh was taken as reference, and it was checked that results do converge quite quickly to the fine mesh as the number of elements increases, see figure B3.

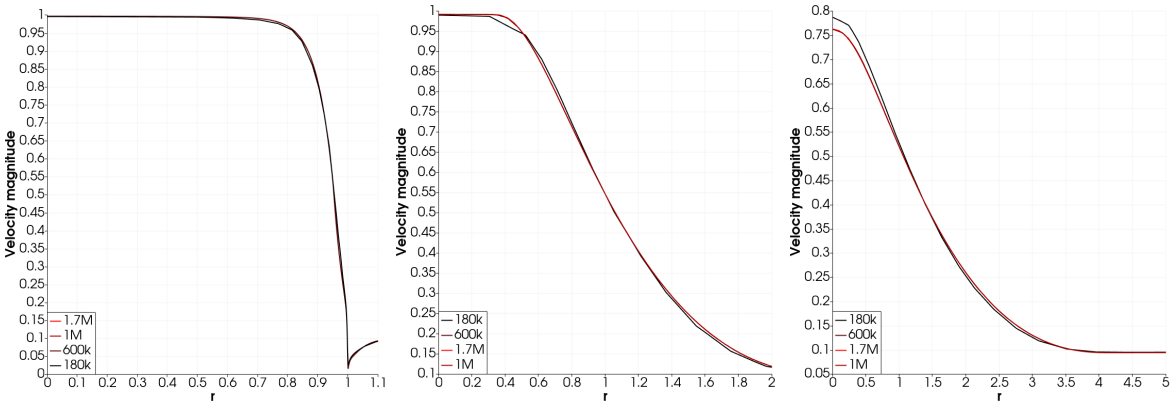

(a) $x = 1 + \epsilon$ (b) $x = 10$ (c) $x = 20$

Figure B3: Velocity magnitude for a variety of slices at different number of elements

References

[1] Leandra I. Abreu et al. "Resolvent modelling of near-wall coherent structures in turbulent channel flow". en. In: *International Journal of Heat and Fluid Flow* 85 (Oct. 2020), p. 108662. ISSN: 0142-727X. DOI: 10.1016/j.ijheatfluidflow.2020.108662. URL: https://www.sciencedirect.com/science/article/pii/S0142727X20305580 (visited on 03/30/2021).

[2] Martin Alnæs et al. "Unified form language: A domain-specific language for weak formulations of partial differential equations". In: *ACM Transactions on Mathematical Software* 40.2 (Mar. 2014), 9:1–9:37. ISSN: 0098-3500. DOI: 10.1145/2566630. URL: https://doi.org/10.1145/2566630 (visited on 06/02/2023).

[3] P. R. Amestoy et al. "A Fully Asynchronous Multifrontal Solver Using Distributed Dynamic Scheduling". In: *SIAM Journal on Matrix Analysis and Applications* 23.1 (2001), pp. 15–41.

[4] P. R. Amestoy et al. "Hybrid scheduling for the parallel solution of linear systems". In: *Parallel Computing* 32.2 (2006), pp. 136–156.

[5] Satish Balay et al. "Efficient Management of Parallelism in Object Oriented Numerical Software Libraries". In: *Modern Software Tools in Scientific Computing*. Ed. by E. Arge, A. M. Bruaset, and H. P. Langtangen. Birkhäuser Press, 1997, pp. 163–202.

[6] Satish Balay et al. *PETSc Web page*. https://petsc.org/. 2023. URL: https://petsc.org/.

[7] Satish Balay et al. *PETSc/TAO Users Manual*. Tech. rep. ANL-21/39 - Revision 3.19. Argonne National Laboratory, 2023.

[8] G. K. Batchelor and A. E. Gill. "Analysis of the stability of axisymmetric jets". en. In: *Journal of Fluid Mechanics* 14.4 (Dec. 1962). Publisher: Cambridge University Press, pp. 529–551. ISSN: 1469-7645, 0022-1120. DOI: 10.1017/S0022112062001421. URL: https://www.cambridge.org/core/journals/journal-of-fluid-mechanics/article/analysis-of-the-stability-of-axisymmetric-jets/AA68EA9CE4714C50B8B087ECA1E2E67B (visited on 08/17/2023).

[9] Samir Beneddine et al. "Conditions for validity of mean flow stability analysis". en. In: *Journal of Fluid Mechanics* 798 (July 2016). Publisher: Cambridge University Press, pp. 485–504. ISSN: 0022-1120, 1469-7645. DOI: 10.1017/jfm.2016.331. URL: https://www.cambridge.org/core/journals/journal-of-fluid-mechanics/article/conditions-for-validity-of-mean-flow-stability-analysis/2B42614C79F7EE9860AA56FB3DF1AB39 (visited on 08/17/2023).

[10] Paul Billant, Jean Marc Chomaz, and Patrick Huerre. "Experimental study of vortex breakdown in swirling jets". en. In: *Journal of Fluid Mechanics* 376 (Dec. 1998). Publisher: Cambridge University Press, pp. 183–219. ISSN: 1469-7645, 0022-1120. DOI: 10.1017/S0022112098002870. URL: https://www.cambridge.org/core/journals/journal-of-fluid-mechanics/article/experimental-study-of-vortex-breakdown-in-swirling-jets/E78D382E75210292513FBEAD98551D75 (visited on 07/28/2023).

[11] Paul Billant and François Gallaire. "A unified criterion for the centrifugal instabilities of vortices and swirling jets". en. In: *Journal of Fluid Mechanics* 734 (Nov. 2013). Publisher: Cambridge University Press, pp. 5–35. ISSN: 0022-1120, 1469-7645. DOI: 10.1017/jfm.2013.460. URL: https://www.cambridge.org/core/journals/journal-of-fluid-mechanics/article/abs/unified-criterion-for-the-centrifugal-instabilities-of-vortices-and-swirling-jets/7DF5272AD53C8552615C36CE2D41C7B6 (visited on 08/02/2023).

[12] Paul Billant and François Gallaire. "Generalized Rayleigh criterion for non-axisymmetric centrifugal instabilities". en. In: *Journal of Fluid Mechanics* 542 (Nov. 2005). Publisher: Cambridge University Press, pp. 365–379. ISSN: 1469-7645, 0022-1120. DOI: 10.1017/S0022112005006464. URL: https://www.cambridge.org/core/journals/journal-of-fluid-mechanics/article/generalized-rayleigh-criterion-for-nonaxisymmetric-centrifugal-instabilities/EBD5A1C0273A1D8616C5F1FC75085DCF (visited on 08/17/2023).

[13] Quentin Chevalier, Lesshafft Lutz, and André V. G. Cavalieri. "A second-order resolvent formulation for the analysis of turbulent flow structures". In: *Comptes Rendus. Mécanique* 351.G2 (2023), pp. 355–371. ISSN: 1873-7234. DOI: 10.5802/crmeca.193. URL: https://comptes-rendus.academie-sciences.fr/mecanique/articles/10.5802/crmeca.193/ (visited on 10/23/2023).

[14] Lisandro Dalcin et al. "Parallel distributed computing using Python". en. In: *Advances in Water Resources*. New Computational Methods and Software Tools 34.9 (Sept. 2011), pp. 1124–1139. ISSN: 0309-1708. DOI: 10.1016/j.advwatres.2011.04.013. URL: https://www.sciencedirect.com/science/article/pii/S0309170811000777 (visited on 05/03/2022).

[15] Christopher M. Douglas, Benjamin L. Emerson, and Timothy C. Lieuwen. "Nonlinear dynamics of fully developed swirling jets". en. In: *Journal of Fluid Mechanics* 924 (Oct. 2021). Publisher: Cambridge University Press, A14. ISSN: 0022-1120, 1469-7645. DOI: 10.1017/jfm.2021.615. URL: https://www.cambridge.org/core/journals/journal-of-fluid-mechanics/article/nonlinear-dynamics-of-fully-developed-swirling-jets/FE28A6F2254BAE7A97058457F4C9E3E5 (visited on 01/12/2023).

[16] P. G. Drazin and W. H. Reid. *Hydrodynamic Stability*. en. Google-Books-ID: GDDhso7XjngC. Cambridge University Press, Aug. 1982. ISBN: 978-0-521-52541-1.

[17] P. W. Duck. "The inviscid stability of swirling flows: Large wavenumber disturbances". en. In: *Zeitschrift für angewandte Mathematik und Physik ZAMP* 37.3 (May 1986), pp. 340–360. ISSN: 1420-9039. DOI: 10.1007/BF00946755. URL: https://doi.org/10.1007/BF00946755 (visited on 07/31/2023).

[18] T. Ellingsen and E. Palm. "Stability of linear flow". In: *The Physics of Fluids* 18.4 (Apr. 1975), pp. 487–488. ISSN: 0031-9171. DOI: 10.1063/1.861156. URL: https://doi.org/10.1063/1.861156 (visited on 08/16/2023).

[19] Kerry A. Emanuel. "A note on the stability of columnar vortices". en. In: *Journal of Fluid Mechanics* 145 (Aug. 1984). Publisher: Cambridge University Press, pp. 235–238. ISSN: 1469-7645, 0022-1120. DOI: 10.1017/S0022112084002895. URL: https://www.cambridge.org/core/journals/journal-of-fluid-mechanics/article/note-on-the-stability-of-columnar-vortices/7FC0E2325B21CD9D5C915E3E8CBBDA6C (visited on 08/04/2023).

[20] F. Gallaire, S. Rott, and J.-M. Chomaz. "Experimental study of a free and forced swirling jet". en. In: *Physics of Fluids* 16.8 (Aug. 2004), pp. 2907–2917. ISSN: 1070-6631, 1089-7666. DOI: 10.1063/1.1758171. URL: https://pubs.aip.org/pof/article/16/8/2907/255971/Experimental-study-of-a-free-and-forced-swirling (visited on 07/31/2023).

[21] François Gallaire and Jean-Marc Chomaz. "Instability mechanisms in swirling flows". en. In: *Physics of Fluids* 15.9 (Sept. 2003), pp. 2622–2639. ISSN: 1070-6631, 1089-7666. DOI: 10.1063/1.1589011. URL: http://aip.scitation.org/doi/10.1063/1.1589011 (visited on 03/17/2023).

[22] François Gallaire and Jean-Marc Chomaz. "Mode selection in swirling jet experiments: a linear stability analysis". en. In: *Journal of Fluid Mechanics* 494 (Nov. 2003). Publisher: Cambridge University Press, pp. 223–253. ISSN: 1469-7645, 0022-1120. DOI: 10.1017/S0022112003006104. URL:

https://www.cambridge.org/core/journals/journal-of-fluid-mechanics/article/mode-selection-in-swirling-jet-experiments-a-linear-stability-analysis/0AD01253D869A87CE781CCEF66C9958A (visited on 12/08/2022).

[23] Xavier Garnaud. "Modes, transient dynamics and forced response of circular jets". en. PhD thesis. Ecole Polytechnique X, June 2012.

[24] Xavier Garnaud et al. "The preferred mode of incompressible jets: linear frequency response analysis". en. In: *Journal of Fluid Mechanics* 716 (Feb. 2013). Publisher: Cambridge University Press, pp. 189–202. ISSN: 0022-1120, 1469-7645. DOI: 10.1017/jfm.2012.540. URL: https://www.cambridge.org/core/journals/journal-of-fluid-mechanics/article/preferred-mode-of-incompressible-jets-linear-frequency-response-analysis/ADB24D98759281E33495286BC5810397 (visited on 12/08/2022).

[25] Christophe Geuzaine and Jean-François Remacle. "Gmsh: A 3-D finite element mesh generator with built-in pre- and post-processing facilities". en. In: *International Journal for Numerical Methods in Engineering* 79.11 (2009). _eprint: https://onlinelibrary.wiley.com/doi/pdf/10.1002/nme.2579, pp. 1309–1331. ISSN: 1097-0207. DOI: 10.1002/nme.2579. URL: https://onlinelibrary.wiley.com/doi/abs/10.1002/nme.2579 (visited on 06/05/2023).

[26] Vicente Hernandez, Jose E. Roman, and Vicente Vidal. "SLEPc: A scalable and flexible toolkit for the solution of eigenvalue problems". In: *ACM Transactions on Mathematical Software* 31.3 (Sept. 2005), pp. 351–362. ISSN: 0098-3500. DOI: 10.1145/1089014.1089019. URL: https://doi.org/10.1145/1089014.1089019 (visited on 09/18/2023).

[27] Louis N. Howard and A. S. Gupta. "On the hydrodynamic and hydromagnetic stability of swirling flows". en. In: *Journal of Fluid Mechanics* 14.3 (Nov. 1962). Publisher: Cambridge University Press, pp. 463–476. ISSN: 1469-7645, 0022-1120. DOI: 10.1017/S0022112062001366. URL: https://www.cambridge.org/core/journals/journal-of-fluid-mechanics/article/on-the-hydrodynamic-and-hydromagnetic-stability-of-swirling-flows/045686729B6B3B5D746510AA8042AA4E (visited on 08/17/2023).

[28] A.K.M.F. Hussain and W.C. Reynolds. "The mechanics of an organized wave in turbulent shear flow". In: *Journal of Fluid Mechanics* 41.2 (1970), pp. 241–258.

[29] Mehdi R. Khorrami. "On the viscous modes of instability of a trailing line vortex". en. In: *Journal of Fluid Mechanics* 225 (Apr. 1991). Publisher: Cambridge University Press, pp. 197–212. ISSN: 1469-7645, 0022-1120. DOI: 10.1017/S0022112091002021. URL: https://www.cambridge.org/core/journals/journal-of-fluid-mechanics/article/on-the-viscous-modes-of-instability-of-a-trailing-line-vortex/1187C024D013542C16B467272A726788 (visited on 07/24/2023).

[30] Mehdi R. Khorrami. "Stability of a compressible axisymmetric swirling jet". In: *AIAA Journal* 33.4 (1995). Publisher: American Institute of Aeronautics and Astronautics _eprint: https://doi.org/10.2514/3.12627, pp. 650–658. ISSN: 0001-1452. DOI: 10.2514/3.12627. URL: https://doi.org/10.2514/3.12627 (visited on 07/24/2023).

[31] S. Leibovich and K. Stewartson. "A sufficient condition for the instability of columnar vortices". en. In: *Journal of Fluid Mechanics* 126 (Jan. 1983). Publisher: Cambridge University Press, pp. 335–356. ISSN: 1469-7645, 0022-1120. DOI: 10.1017/S0022112083000191. URL: https://www.cambridge.org/core/journals/journal-of-fluid-mechanics/article/sufficient-condition-for-the-instability-of-columnar-vortices/1D9BBD70FF45F18D5D5561C9153C2528 (visited on 05/11/2023).

[32] Martin Lessen and Frederick Paillet. "The stability of a trailing line vortex. Part 2. Viscous theory". en. In: *Journal of Fluid Mechanics* 65.4 (Oct. 1974). Publisher: Cambridge University Press, pp. 769–779. ISSN: 1469-7645, 0022-1120. DOI: 10.1017/S0022112074001649. URL: https://www.cambridge.org/core/journals/journal-of-fluid-mechanics/article/stability-of-a-trailing-line-vortex-part-2-viscous-theory/3A330105F65E90DE510E6E96000C9712 (visited on 07/24/2023).

[33] Martin Lessen, Pawan Jit Singh, and Frederick Paillet. "The stability of a trailing line vortex. Part 1. Inviscid theory". en. In: *Journal of Fluid Mechanics* 63.4 (May 1974). Publisher: Cambridge University Press, pp. 753–763. ISSN: 1469-7645, 0022-1120. DOI: 10.1017/S0022112074002175. URL: https://www.cambridge.org/core/journals/journal-of-fluid-mechanics/article/stability-of-a-trailing-line-vortex-part-1-inviscid-theory/5247D9EC899DB3A37379D626C6FD6B87 (visited on 07/24/2023).

[34] Lutz Lesshafft et al. "Resolvent-based modelling of coherent wavepackets in a turbulent jet". en. In: (2019), p. 29.

[35] Hanzhuang Liang and T. Maxworthy. "An experimental investigation of swirling jets". en. In: *Journal of Fluid Mechanics* 525 (Feb. 2005). Publisher: Cambridge University Press, pp. 115–159. ISSN: 1469-7645, 0022-1120. DOI: 10.1017/S0022112004002629. URL: https://www.cambridge.org/core/journals/journal-of-fluid-mechanics/article/an-experimental-investigation-of-swirling-jets/3852557C98F04A0D5925F6F1738213BA (visited on 08/01/2023).

[36] Thomas Loiseleux, Jean-Marc Chomaz, and Patrick Huerre. "The effect of swirl on jets and wakes: Linear instability of the Rankine vortex with axial flow". In: *Physics of Fluids* 10.5 (May 1998). Publisher: American Institute of Physics, pp. 1120–1134. ISSN: 1070-6631. DOI: 10.1063/1.869637. URL: https://aip.scitation.org/doi/abs/10.1063/1.869637 (visited on 03/14/2023).

[37] Thomas Loiseleux, Ivan Delbende, and Patrick Huerre. "Absolute and convective instabilities of a swirling jet/wake shear layer". In: *Physics of Fluids* 12.2 (Feb. 2000). Publisher: American Institute of Physics, pp. 375–380. ISSN: 1070-6631. DOI: 10.1063/1.870315. URL: https://aip.scitation.org/doi/abs/10.1063/1.870315 (visited on 04/04/2023).

[38] Ganyu Lu and Sanjiva K. Lele. "Inviscid instability of compressible swirling mixing layers". In: *Physics of Fluids* 11.2 (Feb. 1999), pp. 450–461. ISSN: 1070-6631. DOI: 10.1063/1.869861. URL: https://doi.org/10.1063/1.869861 (visited on 05/11/2023).

[39] J. E. Martin and E. Meiburg. "Nonlinear axisymmetric and three-dimensional vorticity dynamics in a swirling jet model". In: *Physics of Fluids* 8.7 (July 1996), pp. 1917–1928. ISSN: 1070-6631. DOI: 10.1063/1.868971. URL: https://doi.org/10.1063/1.868971 (visited on 08/21/2023).

[40] J. E. Martin and E. Meiburg. "Numerical investigation of three-dimensionally evolving jets under helical perturbations". en. In: *Journal of Fluid Mechanics* 243.-1 (Oct. 1992), p. 457. ISSN: 0022-1120, 1469-7645. DOI: 10.1017/S0022112092002787. URL: http://www.journals.cambridge.org/abstract_S0022112092002787 (visited on 10/17/2023).

[41] J. E. Martin and E. Meiburg. "On the stability of the swirling jet shear layer". In: *Physics of Fluids* 6.1 (Jan. 1994), pp. 424–426. ISSN: 1070-6631. DOI: 10.1063/1.868041. URL: https://doi.org/10.1063/1.868041 (visited on 08/21/2023).

[42] J. E. Martin and E. Meiburg. "The growth and nonlinear evolution of helical perturbations in a swirling jet model". In: *European Journal of Mechanics - B/Fluids*. Special Issue Dynamics and Statistics of Concentrated Vortices in Turbulent Flow (Euromech Colloquium 364) 17.4 (July 1998), pp. 639–651. ISSN: 0997-7546. DOI: 10.1016/S0997-7546(98)80017-4. URL: https://www.sciencedirect.com/science/article/pii/S0997754698800174 (visited on 08/21/2023).

[43] J. E. Martin and E. Meiburg. "The nonlinear evolution of swirling jets". en. In: *Meccanica* 29.4 (Dec. 1994), pp. 331–341. ISSN: 1572-9648. DOI: 10.1007/BF00987568. URL: https://doi.org/10.1007/BF00987568 (visited on 08/21/2023).

[44] Philippe Meliga, François Gallaire, and Jean-Marc Chomaz. "A weakly nonlinear mechanism for mode selection in swirling jets". en. In: *Journal of Fluid Mechanics* 699 (May 2012). Publisher: Cambridge University Press, pp. 216–262. ISSN: 1469-7645, 0022-1120. DOI: 10.1017/jfm.2012.93. URL: https://www.cambridge.org/core/journals/journal-of-fluid-mechanics/article/weakly-nonlinear-mechanism-for-mode-selection-in-swirling-jets/9C383EFFD22327805E07B6C7355F4C3E (visited on 10/06/2021).

[45] Pradeep Moise and Joseph Mathew. "Hysteresis and turbulent vortex breakdown in transitional swirling jets". en. In: *Journal of Fluid Mechanics* 915 (May 2021). Publisher: Cambridge University Press, A94. ISSN: 0022-1120, 1469-7645. DOI: 10.1017/jfm.2021.118. URL: https://www.cambridge.org/core/journals/journal-of-fluid-mechanics/article/hysteresis-and-turbulent-vortex-breakdown-in-transitional-swirling-jets/5D312B03D1820CCE9A9F75C916A0D666 (visited on 07/31/2023).

[46] D. Montagnani and F. Auteri. "Non-modal analysis of coaxial jets". en. In: *Journal of Fluid Mechanics* 872 (Aug. 2019). Publisher: Cambridge University Press, pp. 665–696. ISSN: 0022-1120, 1469-7645. DOI: 10.1017/jfm.2019.356. URL: https://www.cambridge.org/core/journals/journal-of-fluid-mechanics/article/nonmodal-analysis-of-coaxial-jets/C633433D304F1E8E64EFE849874B8349 (visited on 11/14/2022).

[47] Pierluigi Morra et al. "Resolvent Analysis: With or Without Eddy Viscosity?" en. In: *ERCOFTAC Bulletin* 118 (2019), p. 20. URL: https://hal.science/hal-02348082 (visited on 06/05/2023).

[48] Pierluigi Morra et al. "The colour of forcing statistics in resolvent analyses of turbulent channel flows". en. In: *Journal of Fluid Mechanics* 907 (Jan. 2021). Publisher: Cambridge University Press. ISSN: 0022-1120, 1469-7645. DOI: 10.1017/jfm.2020.802. URL: https://www.cambridge.org/core/

journals/journal-of-fluid-mechanics/article/colour-of-forcing-statistics-in-resolvent-analyses-of-turbulent-channel-flows/CBB737704F659C39772EB1637750E687 (visited on 12/02/2020).

[49] Petronio A. S. Nogueira et al. "Large-scale streaky structures in turbulent jets". en. In: *Journal of Fluid Mechanics* 873 (Aug. 2019). Publisher: Cambridge University Press, pp. 211–237. ISSN: 0022-1120, 1469-7645. DOI: 10.1017/jfm.2019.365. URL: https://www.cambridge.org/core/journals/journal-of-fluid-mechanics/article/abs/largescale-streaky-structures-in-turbulent-jets/B37B6DA58363B19F2DB49B9026D6A40F (visited on 04/29/2022).

[50] K. Oberleithner, C. O. Paschereit, and I. Wygnanski. "On the impact of swirl on the growth of coherent structures". en. In: *Journal of Fluid Mechanics* 741 (Feb. 2014). Publisher: Cambridge University Press, pp. 156–199. ISSN: 0022-1120, 1469-7645. DOI: 10.1017/jfm.2013.669. URL: https://www.cambridge.org/core/journals/journal-of-fluid-mechanics/article/on-the-impact-of-swirl-on-the-growth-of-coherent-structures/3A7F8E35D4213EE83CBD2E07788F1AF7 (visited on 06/26/2023).

[51] J. Panda and D. K. McLaughlin. "Experiments on the instabilities of a swirling jet". en. In: *Physics of Fluids* 6.1 (Jan. 1994), pp. 263–276. ISSN: 1070-6631, 1089-7666. DOI: 10.1063/1.868074. URL: https://pubs.aip.org/pof/article/6/1/263/259492/Experiments-on-the-instabilities-of-a-swirling-jet (visited on 08/03/2023).

[52] Ethan Pickering et al. "Lift-up, Kelvin-Helmholtz and Orr mechanisms in turbulent jets". In: *Journal of Fluid Mechanics* 896 (Aug. 2020). arXiv: 1909.09737, A2. ISSN: 0022-1120, 1469-7645. DOI: 10.1017/jfm.2020.301. URL: http://arxiv.org/abs/1909.09737 (visited on 10/23/2020).

[53] Rayleigh. "On the Dynamics of Revolving Fluids on JSTOR". en. In: *Proceedings of the Royal Society of London.* Vol. 93. Containing Papers of a Mathematical and Physical Character A. Royal Society, Mar. 1917, pp. 148–154. URL: https://www.jstor.org/stable/93794 (visited on 08/17/2023).

[54] Lord Rayleigh. "VIII. On the question of the stability of the flow of fluids". In: *The London, Edinburgh, and Dublin Philosophical Magazine and Journal of Science* 34.206 (July 1892). Publisher: Taylor & Francis _eprint: https://doi.org/10.1080/14786449208620167, pp. 59–70. ISSN: 1941-5982. DOI: 10.1080/14786449208620167. URL: https://doi.org/10.1080/14786449208620167 (visited on 08/17/2023).

[55] J. E. Roman et al. *SLEPc Users Manual.* Tech. rep. DSIC-II/24/02 - Revision 3.20. D. Sistemes Informàtics i Computació, Universitat Politècnica de València, 2023.

[56] Peter J. Schmid. "Nonmodal Stability Theory". en. In: *Annual Review of Fluid Mechanics* 39.1 (Jan. 2007), pp. 129–162. ISSN: 0066-4189, 1545-4479. DOI: 10.1146/annurev.fluid.38.050304.092139. URL: https://www.annualreviews.org/doi/10.1146/annurev.fluid.38.050304.092139 (visited on 12/07/2022).

[57] Oliver T. Schmidt et al. "Spectral analysis of jet turbulence". en. In: *Journal of Fluid Mechanics* 855 (Nov. 2018), pp. 953–982. ISSN: 0022-1120, 1469-7645. DOI: 10.1017/jfm.2018.675. URL: https://www.cambridge.org/core/product/identifier/S0022112018006754/type/journal_article (visited on 08/03/2021).

[58] Matthew Scroggs et al. "Basix: a runtime finite element basis evaluation library". en. In: *Journal of Open Source Software* 7.73 (May 2022), p. 3982. ISSN: 2475-9066. DOI: 10.21105/joss.03982. URL: https://joss.theoj.org/papers/10.21105/joss.03982 (visited on 06/02/2023).

[59] Matthew Scroggs et al. "Construction of Arbitrary Order Finite Element Degree-of-Freedom Maps on Polygonal and Polyhedral Cell Meshes". In: *ACM Transactions on Mathematical Software* 48.2 (May 2022), 18:1–18:23. ISSN: 0098-3500. DOI: 10.1145/3524456. URL: https://dl.acm.org/doi/10.1145/3524456 (visited on 06/02/2023).

[60] Onofrio Semeraro et al. "Modeling of coherent structures in a turbulent jet as global linear instability wavepackets: Theory and experiment". en. In: *International Journal of Heat and Fluid Flow* 62 (Dec. 2016), pp. 24–32. ISSN: 0142-727X. DOI: 10.1016/j.ijheatfluidflow.2016.10.010. URL: https://www.sciencedirect.com/science/article/pii/S0142727X16307056 (visited on 06/15/2023).

[61] P. Spalart and S. Allmaras. "A one-equation turbulence model for aerodynamic flows". In: *30th Aerospace Sciences Meeting and Exhibit.* _eprint: https://arc.aiaa.org/doi/pdf/10.2514/6.1992-439. American Institute of Aeronautics and Astronautics, 1994. DOI: 10.2514/6.1992-439. URL: https://arc.aiaa.org/doi/abs/10.2514/6.1992-439 (visited on 01/25/2022).

[62] L J. Synge. "The stability of heterogeneous liquids". In: *Trans. R. Soc. Canada* 27 (1938), p. 1. URL: https://cir.nii.ac.jp/crid/1570572700002381952 (visited on 08/25/2023).

[63] *The OpenFOAM Foundation*. URL: https://openfoam.org/ (visited on 04/29/2022).
[64] A. Towne, O.T. Schmidt, and T. Colonius. "Spectral proper orthogonal decomposition and its relationship to dynamic mode decomposition and resolvent analysis". In: *Journal of Fluid Mechanics* 847 (2018), pp. 821–867.
[65] Junchao Zhang et al. "The PetscSF Scalable Communication Layer". In: *IEEE Transactions on Parallel and Distributed Systems* 33.4 (2022), pp. 842–853.